A machine learning-based methodology for computational aeroacoustics predictions of multi-propeller drones

Cesar Legendre[1], Vincent Ficat-Andrieu, Athanasios Poulos,
Free Field Technologies,
MSC Software Belgium, Rue Emile Francqui 9 1435 Mont Saint Guibert, Belgium

Yuya Kitano & Yoshitaka Nakashima
Software Cradle Co.
Ltd, 3-4-5, Umeda, Kita-ku Osaka 530-0001, Japan

Wataru Kobayash & Gaku Minorikawa
Hosei University Urban Air Mobility Laboratory
Tokyo, 184-0002, Japan

ABSTRACT

The rapid progress in technological developments of small Unmanned Aircraft Systems (sUAS) or simply "drones" has produced a significant proliferation of this technology. From multinational businesses to drone enthusiasts, such a technology can offer a wide range of possibilities, i.e., commercial services, security, and environmental applications, while placing new demands in the already-congested civil airspace. Noise emission is a key factor that is being addressed with high-fidelity computational fluid dynamics (CFD) and aeroacoustics (CAA) techniques. However, due to uncertainties of flow conditions, wide ranges of propellers' speed variations, and different payload requirements, a complete numerical prediction varying such parameters is unfeasible. In this study, a machine learning-based approach is proposed in combination with high-fidelity CFD and CAA techniques to predict drone noise emission given a wide variation of payloads or propellers' speeds. The transient CFD computations are calculated using a time-marching LES simulation with a WALE sub-grid scale. In contrast, the acoustic propagation is predicted using a finite element method in the frequency domain. Finally, the machine learning strategy is presented in the context of fulfilling two goals: (i) real-time noise prediction of drone systems; and (ii) determination of propeller's rotation speeds leading to a noise prediction matching experimental data.

1. INTRODUCTION

Innovations in the technology of small Unmanned Aircraft Systems (**sUAS**) or simply "drones" have drastically reduced their general costs, from development to operations. This democratization is offering a large variety of possibilities to businesses and citizens while increasing the demands on the use of the already-congested civil airspace [1,2]. Besides, to establish a safe growth of the drone-

---

[1] cesar.legendre@hexagon.com

derived economy, important efforts are underway worldwide to set up an articulate regulatory framework for the use of drones [3,4]. Indeed, a crucial aspect of drone operations is noise. For example, depending on the present ambient noise (e.g. city noise), the noise generated by drones may lead to high perceived loudness and annoyance [5].

Modern numerical techniques may help reduce noise from drones. Undoubtedly, the insights provided by the simulations guide engineers and scientists in the discovery of new strategies leading to quieter drone configurations. A common approach relies on high-fidelity computational fluid dynamics (**CFD**) techniques coupled with solutions of Ffowcs Williams-Hawkings' (**FW-H**) analogy [6] for permeable or solid boundaries [7]. Such a deterministic approach usually requires an *apriori* knowledge of the parameter's values at initial conditions, i.e. rotation speed of each rotor, crosswind, pitch angle of the blades' propeller, etc. Remarkable demonstrations can be found in the literature for drone noise predictions [8] or general multi-propeller aircraft noise calculations [9] requiring 8×10^5 and 2.5×10^5 CPU-hours respectively. In real-world situations, initial conditions may vary over a range or its value is simply unknown. Such a situation renders difficult the task of addressing drone (or in general multi-propeller aircraft) noise using a deterministic approach given the cost of the state-of-the-art computational techniques. This is especially the case for low-cost drones in which the market revenue, the ephemeral product life cycle, and economical components, do not simply justify such an investment.

The present work addresses the noise prediction of drones from a statistical perspective. The statistical approach used relies on a combination of CFD, **CAA** (**C**omputational **A**ero**A**coustics) and machine learning techniques to deal with uncertainties or variations of propeller's rotation speeds. Besides the expected increase of overall noise for higher rotational speeds, the acoustic signature can also change, shifting the tonal and broadband noise components towards high (or low) frequencies. This represents an additional constraint to the present methodology.

This study starts with quantitative and qualitative analyses of the experimental data (section 2) revealing uncertainties at the drone conditions. Then, a machine learning strategy is presented in section 3, followed by the description of CFD (section 4.2) and CAA (section 4.3) techniques. With the data produced by the CFD/CAA processes, a hyper-parameter analysis is performed to determine the best machine learning model (section 5). The best predictor model is presented in the context of fulfilling two goals: real-time noise prediction of drone systems and determination of rotation speed(s) leading to a noise prediction matching experimental data. Finally, the results are discussed and analyzed (section 6) followed by concluding remarks and possible further investigations (section 7).

2. ANALYSIS OF EXPERIMENTAL DATA

The drone used for the measurements is a low-cost (~70$ - May 2021) quadcopter/double propeller *LHI-QAV250* model, very popular among drone enthusiasts. The dimensions of the drone model are depicted in Figure 1a. In the measurements, the drone was attached to a fixed platform at 1.97 m from the floor and 8 measurement points were defined at iso-radius (R = 0.6 m) from the drone's centre of gravity. The measurements were performed on the semi-anechoic chamber facilities at Hosei University Urban Air Mobility Laboratory using a RION NL-31 sound level meter [10].

Usually, low-cost drones are equipped with brushless DC motors with no feedback control to determine the rotation speed. For this reason, the rotation speed is established by the supplied power and then measured using an optical tachometer. Ten different power supplies are considered from 10% to 100% of the maximum power capacity of the battery. Such different power supplies lead to measured rotation speeds in **RPM** (**R**evolution **P**er **M**inute) from 2372 to 18303. For better referencing, the propellers were tagged as (Figure 1b): upper-right (**UR** - red)**,** upper-left (**UL** - green), lower-left (**LL** - blue), and lower-right (**LR** - yellow). The direction of rotation for each propeller is indicated as well

in Figure 1a. Finally, the sound measured was obtained in two different formats, namely spectrum in dBA and as a sound file (*.wav).
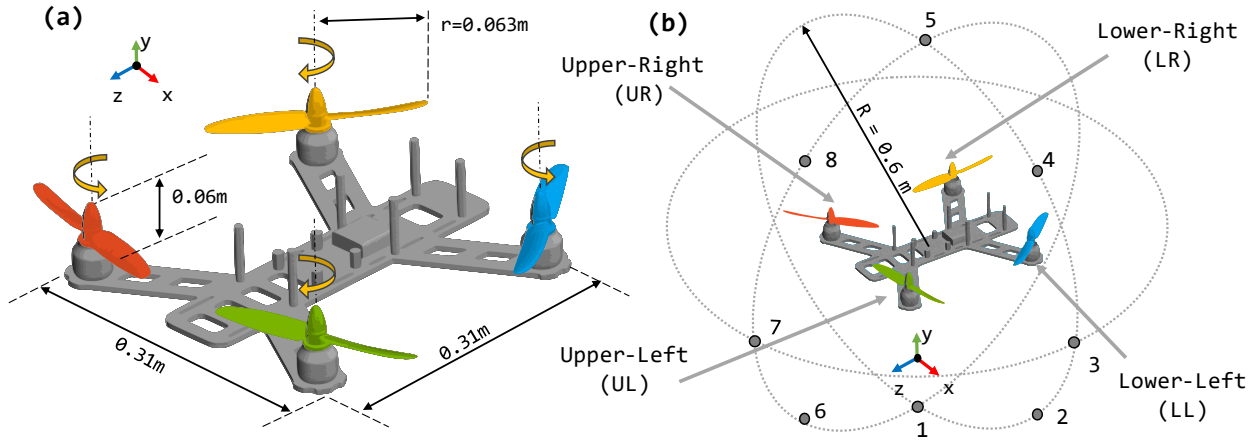

Figure 1: Drone configuration used in measurements and calculations. (a) Dimensions and directions of rotation; (b) Relative position of the microphones (sub-figure not in scale).

Prior to the CFD and CAA calculations, the sound files and the experimental data are analyzed to detect possible anomalies. For instance, for points 1 and 5, an audio inspection revealed a significant blow sound, probably induced by the drone's flow stream at the discharge (point 1) and suction (point 5) sides. This can be observed in the spectrum for point 1 (Figure 2a) and its spectrogram (Figure 2b). Indeed, in contrast to point 1, in point 7 (far from the flow stream), the spectrum (Figure 3a) and spectrogram (Figure 3b) contain well-defined peaks at the rotation speed and harmonics. For practical purposes, such measurement points will be not considered in the numerical comparisons.
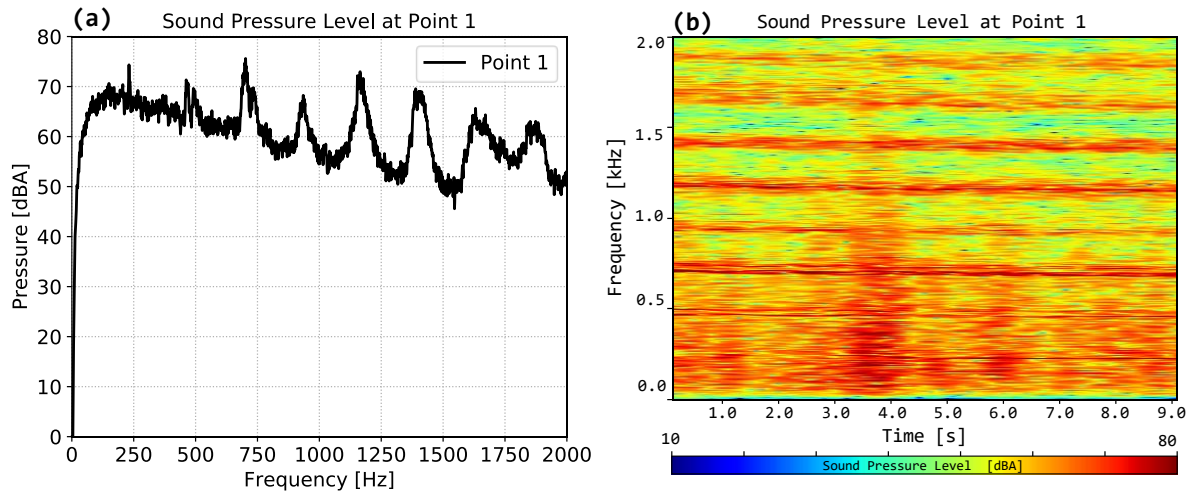

Figure 2: Sound analysis of the *.wav file for point 1 at 18303 RPM measured (100% power capacity). (a) Spectrum. (b) Spectrogram.

Additionally, a closer observation at the spectrum peaks for point 7 (Figure 3a) reveals further irregularities. For instance, the first two peaks in the spectrum and spectrogram (230 Hz and 456 Hz) may correspond to the propeller's rotation speed and its first blade passing frequency (**BPF**) for a rotation speed around ~13800 RPM. Yet, for a rotation speed of 18303 RPM (measured), such peaks should be located at ~305 Hz and ~610 Hz.
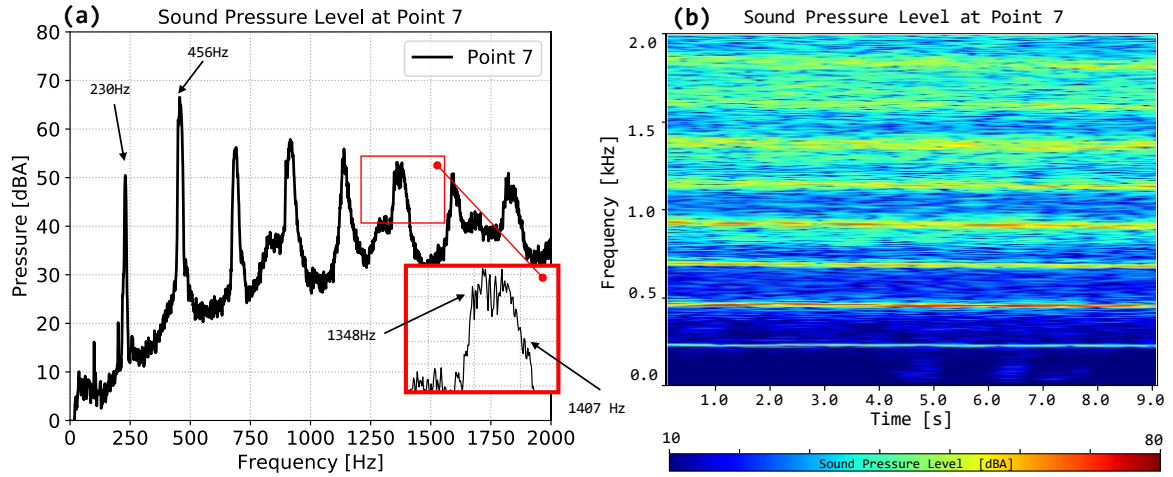
Figure 3: Same as Figure 2 but for point 7.

Besides, another interesting phenomenon is detected by analyzing the relative peak positions in the spectrum. The different peaks start to separate from each other as the frequency increases. For instance, the frequency width of the 6th peak is around 59 Hz ($1407\,Hz - 1348\,Hz$). This may be interpreted as a difference of around ~10 Hz at the 1st harmonic or a ~600 RPM difference between at least two propellers. Such irregularities may be explained by errors in the measurements of the optical tachometer and the difficult control of the rotation speed in low-cost drones.
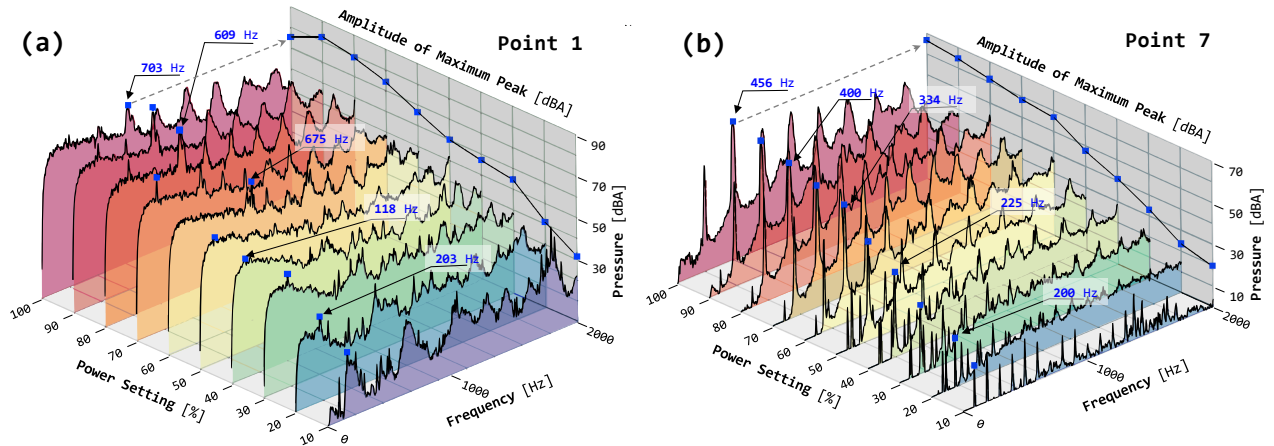

Figure 4: Varying spectra analysis for different power settings of the drone configuration.

A general analysis of the 10 power settings for point 1 and point 7 is observed figure 4. For instance, in figure 4a, as the power increases monotonically, the maximum peaks found (i.e. possible BPF) in the spectra changes in a non-monotonic way. In contrast, for point 7 (figure 4b), the frequency detected for the highest peak (i.e. possible BPF) increases monotonically and the power setting increases.

Consequently, due to the uncertainty of rotation speed values measured by the optical tachometer and the relative difference between the rotation speeds of any pair of propellers, a deterministic CFD and CAA calculation is unfeasible. Therefore, a statistical approach for noise prediction of drones using supervised machine learning techniques is proposed.

3. COMPUTATIONAL STRATEGY BASE ON MACHINE LEARNING

In this section, a machine learning strategy is proposed using acoustics data obtained from CAA and CFD methods. Such a strategy is intended to determine in real-time the noise at different locations produced by the drone given the variation of rotation speed for each propeller.

The general strategy is depicted in Figure 5:. First, CFD calculations using a reduced quarter model are performed by varying the rotation speed from -40% to 0% of deviation from the reference rotation speed selected (18303 RPM). The flow information for each rotation speed (i.e. velocity, pressure and density) is exported to be used in the computation of aeroacoustic sources. Then, the aeroacoustic sources are translated into frequency domain and used in the CAA solver to estimate the sound pressure level up to 5 kHz using 492 discrete frequency values. It is worth noticing that, since the time signal of the flow variables is sufficiently long, this is divided in sub-signals to generate 7 sub-load-cases per rotation speed deviation. Furthermore, given the 9 rotation speed deviations computed for the 4 propellers and 7 sub-load cases, the total amount of realizations carried by the CAA solver raises up to 882 data samples. In other words, the total number of load-cases were computed as $7 \times C(9,4)$ = 882 where C is the combinatorial operator without repetition on the variables (RPMs). Because the data to be used in the machine learning procedure originates from computational physics algorithms, the selection of machine learning features is already determined. Indeed, the features correspond to the deviations of rotation speed for each propeller.
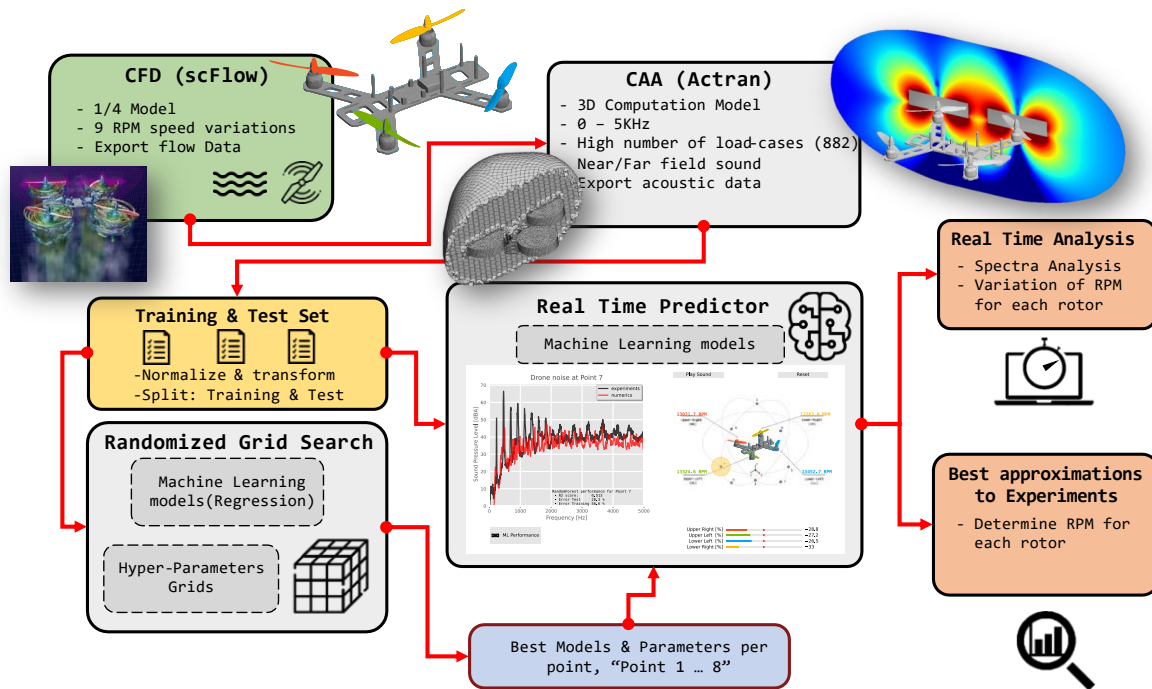

Figure 5: Machine learning strategy in a combination of CAA and CFD simulations.

The 882 data samples from the 8 virtual microphones at 492 discrete frequencies are then divided in two groups, i.e. test and training sets. Such information is first used in the hyperparameter tunning (section 5) for each regressor model selected. For the hyperparameter tuning, a random search is performed to determine the best optimal parameters given an error metric. Finally, two goals to achieved are defined using the best regressor model: (i) a graphical recombination tool is developed to estimate in real-time the noise at each virtual microphone for a user-defined set of rotation speeds; (ii) the combination of rotation speed for each propeller is estimated to minimize the error of the predicted spectrum with respect to the experimental data available.

4. COMPUTATIONAL AEROACOUSTICS AND FLUID DYNAMICS PROCEDURES

4.1. Theoretical Background

Lighthill's rearrangement of fluid dynamics equations into the form of acoustic analogy is written as follows [11,12]:

$$\frac{\partial^2 \rho}{\partial t^2} - c_0^2 \boldsymbol{\nabla}^2 \rho = \boldsymbol{\nabla} \cdot \boldsymbol{\nabla} \, \mathbf{T}_{ij}, \tag{1}$$

the left-hand side (l.h.s) of equation (1) represents a wave equation for the density ρ while the right-hand side (r.h.s.) contains an equivalent source term where $\mathbf{T}_{ij} = \rho u_i u_j + \delta_{ij}(p - c_0^2 \rho) - \tau_{ij}$ is commonly referred as Lighthill's tensor. Furthermore, u_i, p, c_0 and τ_{ij} are the fluid velocity, pressure, speed of sound and viscous tensor respectively, while δ_{ij} is the Kronecker delta. Assuming constant speed of sound c_0, a variational formulation [13] is derived by multiplying equation (1) by a test function ρ^* and integrating over a region Ω as follows:

$$\int_{\Omega} \frac{\partial^2 \rho}{\partial t^2} \rho^* d\Omega - c_0^2 \int_{\Omega} \boldsymbol{\nabla}^2 \rho \rho^* d\Omega = \int_{\Omega} \boldsymbol{\nabla} \cdot \boldsymbol{\nabla} \cdot \mathbf{T}_{ij} \rho^* d\Omega. \tag{2}$$

With $\boldsymbol{\nabla} \cdot (f\boldsymbol{g}) = f\boldsymbol{\nabla} \cdot \boldsymbol{g} + \boldsymbol{g} \cdot \boldsymbol{\nabla} f$, the spatial derivative can be transferred to the test function ρ^* leading to:

$$\int_{\Omega} \frac{\partial^2 \rho}{\partial t^2} \rho^* d\Omega + c_0^2 \int_{\Omega} \boldsymbol{\nabla}\rho^* \cdot \boldsymbol{\nabla}\rho \, d\Omega - c_0^2 \int_{\Omega} \boldsymbol{\nabla} \cdot (\rho^* \boldsymbol{\nabla}\rho) d\Omega$$
$$= -\int_{\Omega} \boldsymbol{\nabla} \cdot \mathbf{T}_{ij} \cdot \boldsymbol{\nabla}\rho^* \, d\Omega + \int_{\Omega} \boldsymbol{\nabla} \cdot (\rho^* \boldsymbol{\nabla} \cdot \mathbf{T}_{ij}) d\Omega. \tag{3}$$

Using Gauss's theorem, i.e. $\int_{\Omega} \boldsymbol{\nabla} \cdot \boldsymbol{g} \, d\Omega = \oint_{\Gamma} \boldsymbol{g} \cdot \mathbf{n} \, d\Gamma$, the last terms at both sides of equation (3) are re-written as surface integrals and regrouped, therefore:

$$\int_{\Omega} \frac{\partial^2 \rho}{\partial t^2} \rho^* d\Omega + c_0^2 \int_{\Omega} \boldsymbol{\nabla}\rho^* \cdot \boldsymbol{\nabla}\rho \, d\Omega = -\int_{\Omega} \boldsymbol{\nabla} \cdot \mathbf{T}_{ij} \cdot \boldsymbol{\nabla}\rho^* \, d\Omega + \oint_{\Gamma} \rho^*(\boldsymbol{\nabla} \cdot \mathbf{T}_{ij} + c_0^2 \boldsymbol{\nabla}\rho) \cdot \mathbf{n} \, d\Gamma, \tag{4}$$

part of integrant in the surface integral of equation (4), i.e. $\boldsymbol{\nabla} \cdot \mathbf{T}_{ij} + c_0^2 \boldsymbol{\nabla}\rho$ may be expressed as $\boldsymbol{\nabla} \cdot (\rho u_i u_i + \delta_{ij}p - \tau_{ij}) = -\partial(\rho u_i)/\partial t$ corresponding to the time derivate of the momentum ρu_i. Therefore, equation (4) is finally expressed as:

$$\int_{\Omega} \frac{\partial^2 \rho}{\partial t^2} \rho^* d\Omega + c_0^2 \int_{\Omega} \boldsymbol{\nabla}\rho^* \cdot \boldsymbol{\nabla}\rho \, d\Omega = -\int_{\Omega} \boldsymbol{\nabla} \cdot \mathbf{T}_{ij} \cdot \boldsymbol{\nabla}\rho^* \, d\Omega - \oint_{\Gamma} \rho^* \left(\frac{\partial \rho \boldsymbol{u}}{\partial t}\right) \cdot \mathbf{n} \, d\Gamma. \tag{5}$$

The variational formulation of Lighthill's analogy contains two terms, a volume term referred as Lighthill Volume and a surface term or Lighthill Surface. This variational formulation is useful in the context of finite element method (**FEM**) and CAA. For instance, the volume integral only requires first spatial derivatives from the flow solution, convenient for standard low spatial order CFD techniques. Besides, the surface integral only requires first-order time derivatives of the flow information, straightforward in the frequency domain. Furthermore, such a surface integral vanishes: (i) at the solid walls ($\boldsymbol{u}.\boldsymbol{n} = 0$) coinciding with the natural rigid wall conditions for acoustics in FEM or non-slip wall condition in CFD; and (ii) in the far field where sources from turbulence are inexistent.
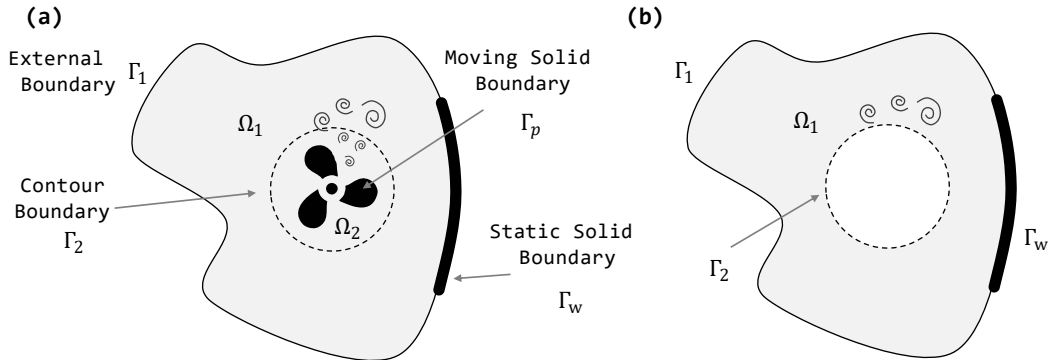

Figure 6: Examples of bounded physical domains. (a) With and (b) without a propeller region.

For instance, considering a bounded computational domain depicted in Figure 6a. According to the variational formulation expressed in equation (5): (i) Lighthill Volume terms are present on Ω_1 and Ω_2 regions; (ii) Lighthill Surface terms vanish at the external boundary Γ_1, the solid wall Γ_w, and

at the moving wall Γ_p with respect to the moving frame of reference; and (iii) do not exist on the contour boundary Γ_2 because Ω_1 and Ω_2 regions are continous. An alternative modelling approach is presented in Figure 6b in which the rotating region Ω_2 is removed. In this case, a surface source or Lighthill Surface appears due to the spatial truncation. This second approach has some advantages: (i) simplifies the modelling by removing the moving parts (propeller), especially for acoustics FEM in frequency domain; (ii) can be arbitrarily placed near the rotating bodies; and (iii) relies on correct flow information, i.e. acoustics and hydrodynamics must be carried by the CFD technique up to such a surface. The latter condition is usually fulfilled because meshes near rotating walls or inside rotating domains need to be sufficiently refined for numerical stability reasons. Such a variational concept, here referred as Lighthill Surface, will be used in a combination with high-fidelity CFD data to model the presence of drone's propellers to later determine their characteristic acoustic signature in near and far field conditions.

4.2. Computational Fluid Dynamics Simulations

The CFD simulation is performed using scFLOW v2021 [17] solver. Calculations were performed on two configurations, a full 3D model with four propellers and a quarter model with one propeller and two symmetry boundary conditions. The computational domain is represented by a volume of dimensions 2.8 m $\times$ 2.8 m $\times$ 3.1 m with two main boundary conditions at its sides: a stress-free on the top and bottom sides and outlet boundary conditions (pressure outlet) at the other sides. Besides, for modelling the propellers, four rotating domains are placed in connection with the static domains by using sliding meshes. Inside each rotating domain, the blade surfaces are modelled as non-slip boundary walls in the rotating frame of reference.
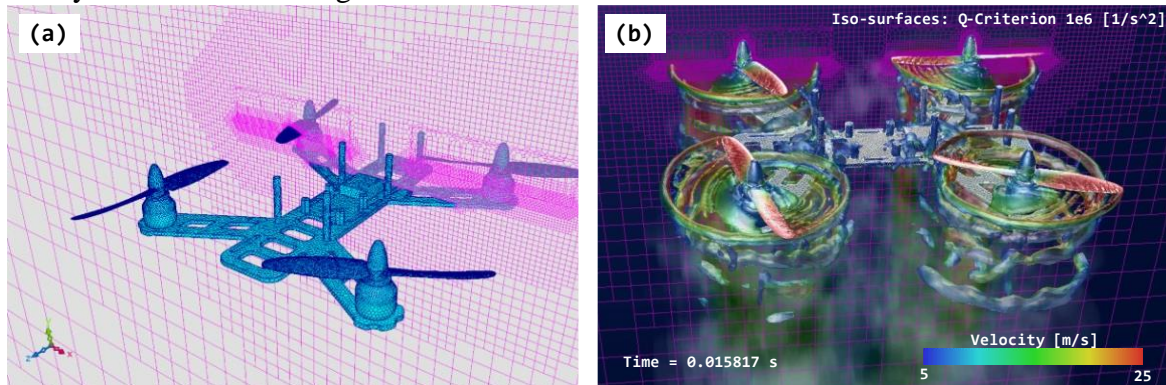

Figure 7: (a) Detail of the CFD mesh. (b) Instantaneous norm of the velocity and Q-criterion at t=0.015817s.

The fluid is air at 20°C with constant density $\rho_0 = 1.205$ kg/m^3, speed of sound $c_0 = 343.6$ m/s and dynamic viscosity $\mu = 1.83 \times 10^{-5}$ Pa. s. An incompressible pressure-based LES solver with **WALE** (Wall-Adapting Local Eddy-Viscosity) sub-grid scale turbulence model was used with a time step of $\Delta t = 2.2765 \times 10^{-6}$ s. The solution of an equivalent steady RANS calculation is set as initial condition for the LES simulation. The mesh for the full model (Figure 7a) consists of 2.7×10^6 polyhedral and hexahedral (voxel) cells while for the quarter model, the mesh contains around 7.0×10^5 cells. In Figure 7b, the instantaneous flow solution for the full propeller configuration with 18303 RPM for each propeller is presented.

As a first step, since the rotation speed of each propeller is unknown, the quarter model is validated to reduce the computational cost of the CFD simulation. Indeed, because the quarter model contains significantly less cells than the full model, its computational cost (~1163 CPU-hours) is reduced (~7550 CPU-hours for full model). In Figure 8a, the instantaneous lift computed from the full model (black line) and four times the lift from the quarter model (red line) are depicted. The lifts computed

are very similar, the average lift difference between the full model (~10.67 N) and the quarter model (~10.71 N) is not greater than 0.37%. Furthermore, the lift spectra (Figure 8b) allow observing further similarities in the frequency content between both CFD models. Given such similarities and lower computational cost, a more refined quarter model (1.1×10^6 cells , ~3160 CPU-hours) is used in the aeroacoustic computations with 9 rotation speeds varying from -40% to 0% from the reference value (i.e. 18303 RPM). Such simulations are performed for 10^5 time steps or 87 propeller rotations) discarding the first 8 rotations to ensure capturing the physics in the established regime. For all the CFD computations a cluster architecture composed of Intel Xeon Gold 6140 @ 2.3 GHz processors was used.
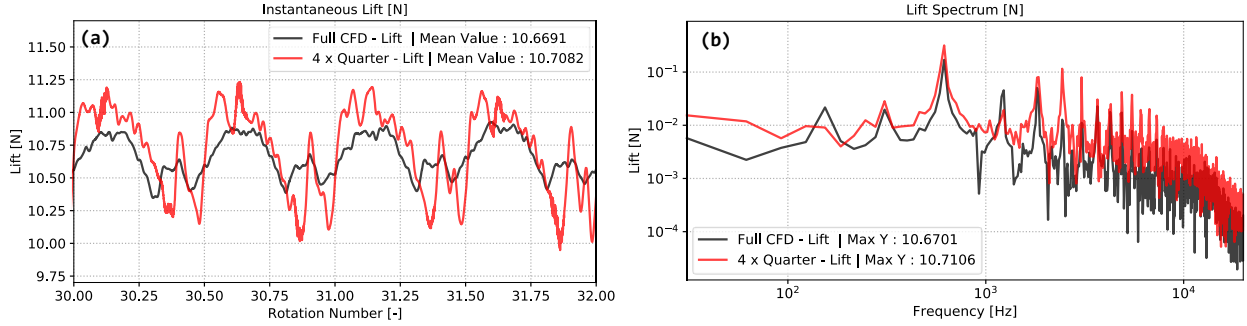

Figure 8: Instantaneous lift using the full CFD model (black line) and the quarter model (red line). (b) time evolution between the 30th and 32nd rotation of the propellers. (b) spectra for the instantaneous lifts.

4.3.   Computational AeroAcoustic Simulations

The acoustic propagation of aerodynamic sources generated by the four propellers is now addressed. The drone is immersed in a fluid at rest placed in a semi-anechoic space. To model the ground effects, mirror virtual microphones are considered. The fluid media for the propagation of the acoustic waves is assumed homogeneous with constant mass density and speed of sound (same as in the CFD model). The acoustic solution is computed using Actran [16] by solving the variational FEM formulation of Lighthill's analogy (section 4.1) in the frequency domain.
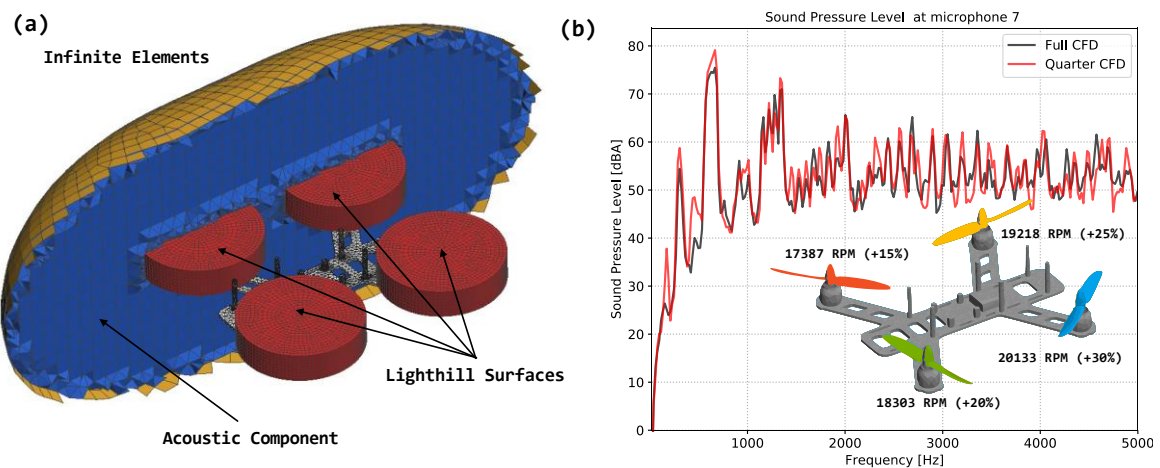

Figure 9: CAA models and results. (a) numerical mesh and components used in Actran simulation. (b) Acoustic validation of the full model CFD data vs. 1/4 CFD data at microphone 7 at different propellers speeds.

A unique acoustic model for the full drone is used (Figure 9a). The aerodynamic sources propagating into the acoustic component and surrounding each propeller are modelled using four Lighthill Surfaces (in red, Figure 9a). The acoustic component (in blue, Figure 9a) is enclosed by infinite

elements [14] (in yellow, Figure 9a, with order $\geq$10) acting as a non-reflecting boundary condition and also serving to calculate the wave solution in the far field. The model is valid up to a computational frequency of 5kHz. The mesh is composed by 4.12×10^5 nodes and 2.48×10^5 elements leading to 5.09×10^5 degrees of freedom. The computation is carried out by Actran 2021 using the MUMPS in-core solver with 4 processes and 4 threads per process (Intel(R) Xeon(R) CPU E5-2697 v4 @ 2.30GHz). The computation time per frequency is around 1min 25s and the maximum consumed RAM per process reaches 36 GB leading to a total computational cost around ~185 CPU-hours for the total 492 frequencies.
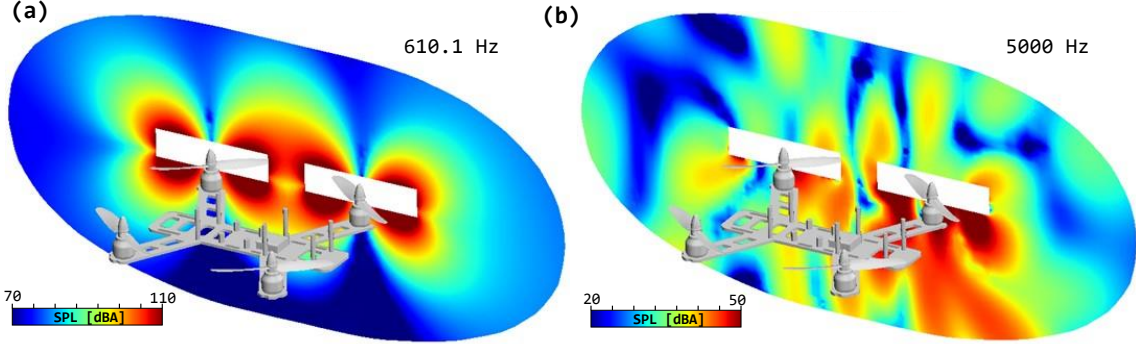

Figure 10: Pressure maps in dBA for 610.1 Hz (BPF) and 5000Hz. The four propellers rotate at 18303 RPM.

Similar to section 4.2, the validation the quarter model with respect to the full CFD model is performed but now with acoustical relevant metrics. In Figure 9, two acoustic computations are compared for point 7: (i) in black, an acoustic computation using a full CFD model with asymmetry in the rotation speed of the propellers as: +5% for UR (17383 RPM), 0% for UL (18303 RPM), +10% for LL (20133 RPM) and +5% (19218 RPM) for LR; (ii) in red, an acoustic computation using 4 different quarter CFD models placed at each one of *Lighthill Surfaces* to emulate the full CFD model. The similarities of both curves are acceptable validating the use of a quarter model for the aeroacoustic computations. As an example, acoustic maps at two frequencies (610.05 Hz or BPF at 18303 RPM) and 5kHz are depicted in Figure 10a,b. Finally, to generate the data to be used to train the machine learning algorithm a full 3D acoustic simulation will be used with all the permutations of 9 rotation speeds (from -40% to 0% deviation) and four propellers.

5. SUPERVISED LEARNING AND HYPERPARAMETER TUNNING

For each virtual microphone spectrum, a prediction model is chosen among the following five regression algorithms using scikit-learn package [15]: (i) Randomized decision trees or Extra-Trees (**ET**); (ii) Random forest (**RF**); (iii) Gradient Boosting (**GB**); (iv) Adaptive Boosting (**AB**); and (v) Support Vector Machine (**SVM**). Such a selection is based on their popularity and common use in the literature. Furthermore, the quality of predictions of those regressors depends on two main factors, the data to be used to train the model (computed by CAA and CFD simulations, see sections 4.2 and 4.3) and a series of optimal hyperparameters specific to each regressor. To obtain such hyperparameters a k-fold (k=5) cross-validation randomized grid search was performed.

To perform the cross-validation, the numerical data was divided in two groups: (i) a training set with 80% of the calculations; and (ii) a test set with the other 20% remaining. The hyperparameters to be optimized for each regressor are summarized in Table 1. The selection of the algorithm as well as the optimal hyperparameters is done by using the mean absolute error (**MAE**) as the reference metric. This metric is selected due to the natural way of interpreting the results of the cross-validation and for its suitability for regression problems. The cross-validation study is performed on point 7, which contains unpolluted acoustic results as explained in section 2.

Regressor	Hyper Parameters Grid
Extra Trees (ET)	**Number of estimators**: 5-2000; **Max depth**: 5-20; **Minimum samples on leaf**: 10-100.
Random Forest (RF)	**Number of estimators**: 50-2000; **Max depth**: 5-20; **Minimum samples on leaf**: 10-100.
Gradient Boosting (GB)	**Number of estimators**: 50-1000; **Max depth**: 1-20; **Sub-samples**: 0.1-0.95; **Learning Rate**: 0.001-0.1 log uniform distribution
Ada Boosting (AB)	**Number of estimators**: 50-1000; **Learning Rate**: 0.001-1.0, log uniform distribution
Support Vector Machine (SVM)	**Regularization parameter (C)**: 1-1000, log uniform; **Kernel coefficient (gamma)**: 0.0001-0.1, **Kernel**: radial basis function (rbf) and linear.

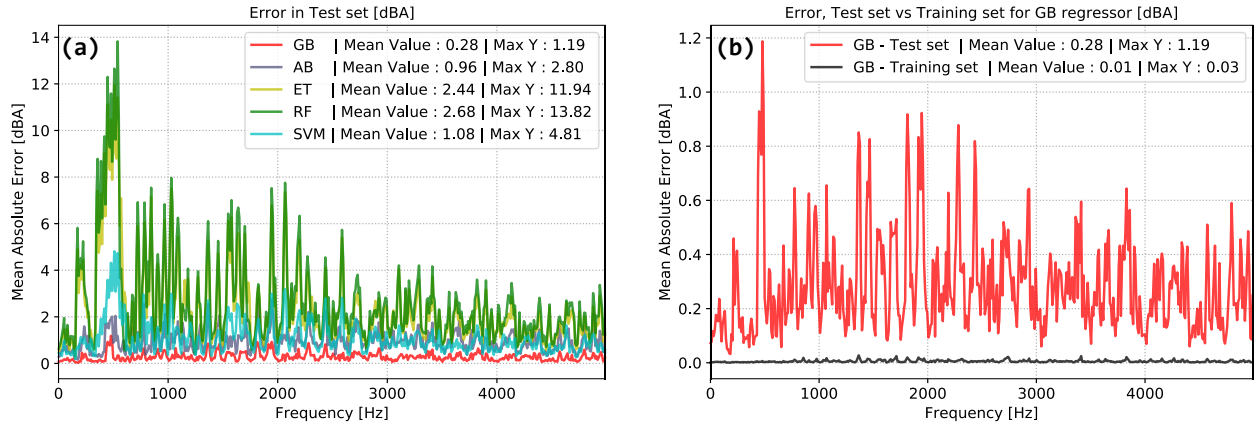Table 1: Hyperparameter grid for each regressor model.

Figure 11: MAE for regressor models using the best hyperparameters at point 7. (a) MAE in test set [dBA] for each model chosen. (b) MAE in test and training sets for GB regressor (selected model).

The randomized grid search allowed to determine the best regressor models (with their hyperparameters) of each class given the selected error metric, i.e. MAE in dBA. The MAE obtained for each regressor model is plotted for point 7 in Figure 11a at each frequency. For the best regressor model (GB), the maximum absolute error estimated is around 1.19 dBA, quite low for acoustics comparison standards.
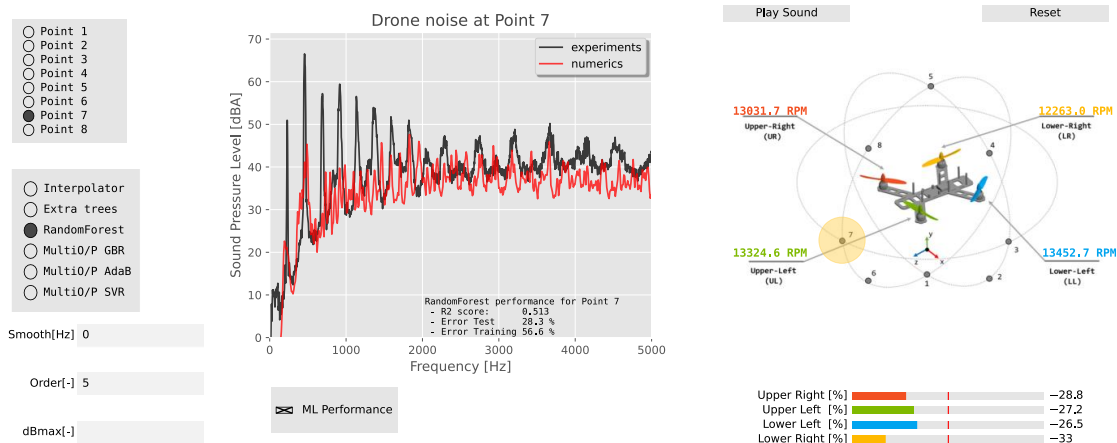

Figure 12: A graphical recombination tool to generate noise results in real-time based on machine learning techniques.

Furthermore, the calculation of the maximum absolute error in the test and training set (Figure 11b) denotes a good fit, i.e. both errors are low enough with test error slightly higher than the training error. This best regressor will be used in the next section for the predictions.

6. POSTPROCESSING AND RESULT PREDICTIONS

Using the best regressor(s) computed in section 5, a recombination tool for rapid noise computation was developed as depicted in Figure 12. The machine learning objects (regressors with the best parameters) are pre-computed and stored to be later loaded in the application. Then, the user may investigate in real-time which rotation speed variation for each propeller generates any change in the drone's acoustic signature at any given point. Besides, the technical analysis of classic dBA vs. frequency curves, it is also possible for the user to listen to the experimental sound (from measurements) and to see the relative position of the measured point with respect to the drone for a better perspective.
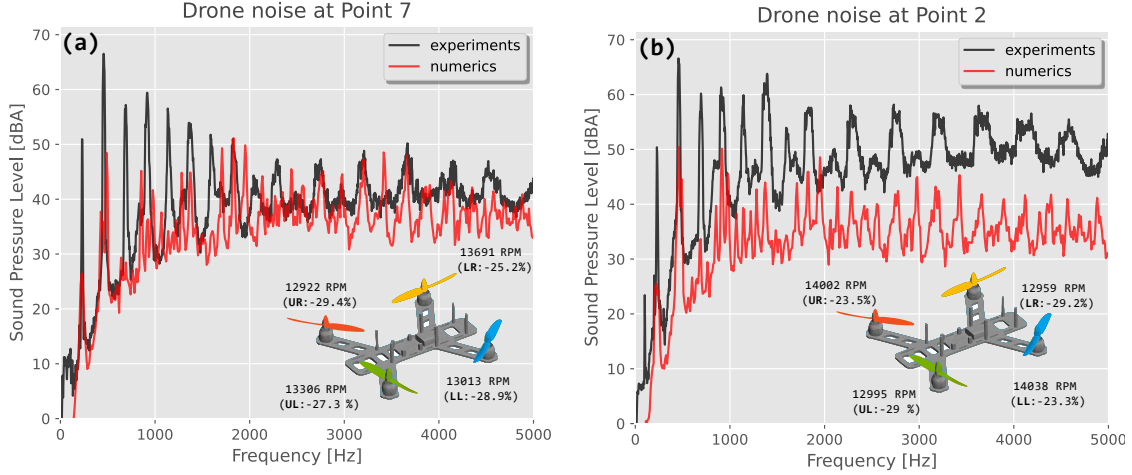

Figure 13: Prediction for power setting measured at 18303 RPM. (a) local optimal close to experimental values for point 7; (b) local optimal close to experimental values for point 2.

As a second goal, the best regressor model is used to determine which variation of rotation speeds approaches the best to the experimental data. Such a minimization problem is addressed as follows: (i) first, with frequency of the highest amplitude peak from the experimental data (BPF), the expected rotation speed is computed; (ii) using such a value as numerical seed, a grid search around -5% and +5% of deviation is performed; (iii) the deviation values leading to a local minimum between the experimental data and predicted spectrum are selected. In addition, the choice of a grid search method is preferred rather than classic minimization algorithms (i.e. gradient descent) because the derivative of the regression functions is not guaranteed to be continuous. Due to physical space in the present publication, only the experimental values corresponding to the highest power supply (measured ~18303 RPM) are presented. In Figure 13a, the numerical prediction and experiments are presented for point 7 for the optimal rotation speeds. It can be observed that, the predictions reconstructed with the regression algorithm match well the experimental data, i.e. several peak's amplitudes are retrieved (including the first two peaks) and general the trend is obtained in the whole frequency range. In addition, it is worth noticing that the prediction model can retrieve the first peak around the rotation speeds. Such a peak emerges due to acoustic interactions of propellers at slight deviations in the rotation speeds. Furthermore, as shown in Figure 13b, the prediction and experiments are compared for point 2. In this comparison, the results match in the frequency prediction of the two first peaks (rotation speed and 1st BPF), however the broadband trend of the predictions values diverges from the experimental results. One explanation of this is the lack of sufficient broadband noise computed in the CAA+CFD step, usually improved as the CFD mesh size decreases.

7. CONCLUSIONS

A combined CAA, CFD and machine learning methodology was proposed to address drone noise calculations given the uncertainties of the rotation speed values. Such uncertainties are common in real-world conditions for low-cost drone systems. Indeed, a deterministic approach would be unfeasible in such configurations because it may lead to a large combination of cases to be computed. The methodology relies on high-fidelity CFD solutions to be later used to compute aeroacoustic sources being propagated by a CAA-FEM solver in frequency domain. The acoustic solution is then treated

as input data to train the machine learning models (regressors) for further predictions. Besides, the best selected regressors in combination with a visual application allow a real-time results reconstruction given the values of rotation speeds for each propeller. Such a rapid recombination has proven to be very useful to understand the behavior of a physical system subjected to a change of input conditions. Furthermore, using the best predictor, the optimal rotation speed values of each propeller was estimated so that minimizes the absolute error with respect to the experimental data. Finally, future works include: (i) to generate sounds (e.g. *.wav files) from the acoustic predictions and maps to visualize the propagation in real-time; (ii) to include other effects of such as pitch variation of blades, installation effects, cross-wind, etc; and (iii) apply the methodology to other multi-propeller aircrafts configurations, e.g. passenger drones, fixed-wing aircrafts with disturbed propulsion, among others.

8. REFERENCES

1   SESAR J.U. (2016). European drones outlook study. Unlocking the value for Europe. *SESAR*, Brussels.
2.   SESAR J.U. (2020). Supporting safe and secure drone operations in Europe. *SESAR*. Brussels.
3.   D. Taurino (2019). AW Drones – Drones Awareness – Project Overview. *European Commission*. Brussels.
4.   Federal Aviation Administration, USA (2021). Operation of Small Unmanned Aircraft Systems Over People, A Rule by the Federal Aviation Administration, published on 01/15/2021.
5.   Torija, A. J., Li, Z., & Self, R. H. (2020). Effects of a hovering unmanned aerial vehicle on urban soundscapes perception. *Transportation Research Part D: Transport and Environment*, **78**, 102195.
6.   Ffowcs-Williams, J. E., and Hawkings, D.L. Sound Generation by Turbulence and Surfaces in Arbitrary Motion . *Phil. Trans. Roy. Soc. (London). Serie A, Math. and Phys. Sci*. **638** 1969, 264, 321–342.
7.   Farassat, F. (2007). Derivation of Formulations 1 and 1A of Farassat. *NASA Technical report*.
8.   Cadieux, F., Barad, M., Jensen, J., & Kiris, C. (2019). Predicting Quadcopter Drone Noise Using the Lattice Boltzmann Method. *NASA Ames Research Center*.
9.   Casalino, D., van der Velden, W. C., Romani, G., & Gonzalez-Martino, I. (2019). Aeroacoustic analysis of urban air operations using the LB/VLES method. In *25th AIAA/CEAS Aeroacoustics Conference* (**p. 2662**).
10. W. Kobayashi (2019). Drone noise measurement for urban air mobility noise assessment (in Japanese). *Master thesis at Hosei University*. Under supervision of G. Minorikawa.
11. Lighthill, M. J. On sound generated aerodynamically. I. General theory. *Proc. Roy. Soc. (London) A-Math. Ph.,* **211**(1107), 564-587, (1952).
12. Lighthill, M. J. On sound generated aerodynamically. II. Turbulence as a source of sound. *Proc. Roy. Soc. (London) A-Math. Ph.*, **222**(1148), 1-32, (1954).
13. A. Oberai, F. Ronaldkin, and T. Hughes. Computational procedures for determining structural-acoustic response due to hydrodynamic sources. *Comp. Methods in Appl. Mech. and Engineering*, **190**:345–361, 2000
14. Astley, R. J., and J-P. Coyette. Conditioning of infinite element schemes for wave problems. *Comm. In Numerical Methods in Engineering* **17**, no. 1, 31-41, (2001).
15. Pedregosa, F., et al. (2011). Scikit-learn: Machine Learning in Python. *J. of Machi. Learn. Research*, **12**, 2825-2830.
16. Free Field Technologies S.A. *Actran 2021 User's Manual*, (2020).

17   Software Cradle Co. scFLOW Version 2021, *User's Guide*, Basic of CFD Analysis. 2020